3
Dimensionally controlled titania at sub-zero temperature, ZnO-TiO_2 and H-HfO_2/TiO_2 nanospheres

Synthetically tuned nanomaterials are presently under intense investigation as they exhibit a wide change in structural, optical and electrical properties. Titania is one of the extensively studied material because of its wide applications. It has been synthesized by various methods from bulk to nanoparticles. Particularly, nano-titania has extensive applications in solar energy harvesting [O'Regan and Gratzel, 1991], catalysis [Hoffmann, Martin, Choi and Bahnemann, 1995; Wang, *et al.*, 2015], hydrogen production and storage [Ni, *et al.*, 2007], and biomedical applications [Kern, *et al.*, 2006; Lima and Marple, 2007]. Notably, synthetically challenging TiO_2 nanorods and nanocrystallite have found to be promising materials. Nanorods have pointed application in the area of water splitting and photovoltaic devices as it provides a direct path for electron transport which improves the charge separation [Leschkies, *et al.*, 2007] while nanocrystals are involved in direct physical applications in paints [Linsebigler, *et al.*, 1995], separation technology [Chen and Mao, 2007], and sensors because of the higher surface area.

Titania nanoparticles are found in nature with three crystalline structures: anatase (tetragonal), rutile (tetragonal) and brookite (orthorhombic), in addition to these, high pressure monoclinic and orthorhombic also exist [Goresy, *et al.*, 2001; El Goresy, *et al.*, 2001]. Anatase converts to rutile at high temperature [Madras, *et al.*, 2007]. Initially, TiO_2 tends to nucleate in anatase form because of significant free energy difference in two phases [Ding, *et al.*, 2010]. The thermal stability and phase transformation of TiO_2 is influenced by the atomic arrangement, packing [Wang and Ying, 1999] and defects [Burns, *et al.*, 2004] and neighboring phase.

3.1 DIMENSIONALLY CONTROLLED TITANIA AT SUB-ZERO TEMPERATURE (-40°C TO -10°C)

Titania nanostructures have been reported using various synthetic methods such aerosol, sol-gel, hydrothermal, inert gas condensation and laser process [Nagaveni, *et al.*, 2004]. These synthetic methods resulted in TiO_2 nanostructure with varied morphologies and shapes e.g. crystals, rods, wires and tubes [Miao, *et al.*, 2002; Zhou and Antonietti, 2003]. It has been reported that highly reactive titanium precursors usually give variable crystalline structure due to poor control on reactivity [Leyva-Porras, *et al.*, 2015]. Controlled growth of TiO_2 nanocrystals has been obtained by modulating hydrolysis rate using surfactant additives [Jin, *et al.*, 2015]. Some of these processes yield quality product under special conditions like high temperature, ultra-high vacuum and, high calcination temperature, making the process cumbersome. It is need of time to have easy processes to synthesize high-quality product at ambient conditions free from any additives. Temperature variation is one of the important parameter studied for controlling nanostructure of TiO_2. Sol-gel is one of the most studied method to prepare various forms of nano-titania at low temperature e.g. Cantau et al, Mutuma and co-workers and Burunkaya et al. reported anatase, rutile and brookite respectively along with other forms in minor quantity [Cantau, *et al.*, 2010; Mutuma, *et al.*, 2013]. In the majority of reports, room temperature (25°C) is described as low temperature [Li, Zhu, Wang, Wang, Guo and Li, 2015; Jiang, *et al.*, 2011; Lai, *et al.*, 2012]. The lowest synthetic temperature ever reported is 4°C

[IRENA, 2012; Burunkaya, *et al.*, 2013] and studies on preparation of titania at sub-zero temperatures (< 0°C) are virtually absent in the literature.

A substantial work was carried out to synthesize nano-titania at sub-zero temperatures to controlled size and morphology. The reaction was performed using TTIP as a precursor with ethanol, water and nitric acid at controlled temperatures from -40 to -10°C (Appendix I) as demonstrated in Figure 1. It is a simple and unique additive free synthetic method to prepare both nanocrystals and nanorods structures at sub-zero temperature using easily accessible chemicals. The role of sub-zero reaction temperature from -40 to -10°C on the structure of TiO_2 and phase transformation between anatase to rutile have been investigated. The current work also throw light on the role of temperature in dimension control of titania nanostructures. The factors like phase conversion, particle size, various defect densities produce strain in the grain boundaries, surface area, nucleation and growth rates and band gap have been explored as they affect the morphology of TiO_2 at sub-zero temperature.

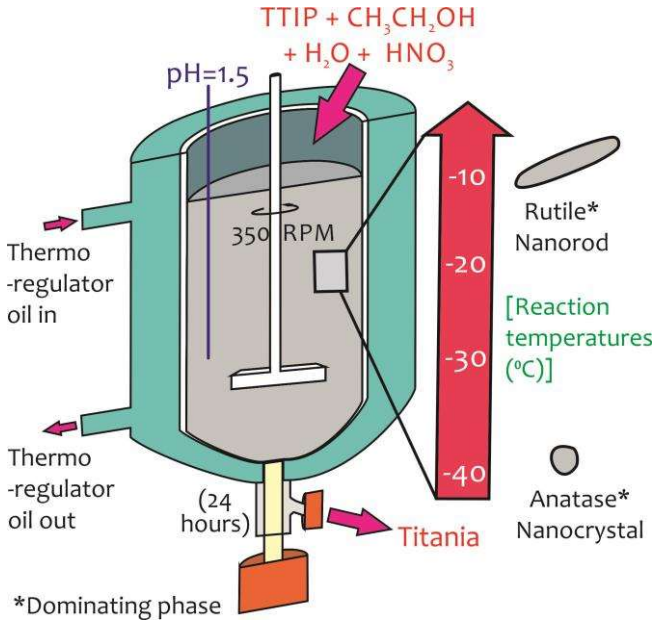

Figure 3.1 : Schematic illustration of nano-TiO_2 synthesis using reactor at temperatures ranging from -40°C to -10°C

3.1.1 Mechanism of titania synthesized at sub-zero temperature

At sub-zero temperature, difference in the particles size and shape originates from crystal structure consisting different arrangement in TiO_6 octahedral units; anatase (zigzag packing) and rutile (linear packing) shown in Figure 3.2.

Small crystal nuclei of both TiO_2 structure will form depending on the surrounding temperature [Yu, *et al.*, 2013; Jun, *et al.*, 2006; Peng, *et al.*, 1998; Manna, *et al.*, 2000]. In anatase, cis-coordination and in rutile trans-coordination sites of octahedral are used for crystal growth. Some have reported that the phase and shape of the TiO_2 nanoparticles formed from crystal growth are governed by anions and solvents [Yang, *et al.*, 2008; Yang, *et al.*, 2009; Jun, *et al.*, 2003]. As temperature increases, the thermal conditions are able to form closest linear packing of the TiO_6 octahedral units [Yan, *et al.*, 2005]. In our case as shown schematically in Figure 3.2 at transition initiation temperature of -10°C, mostly rutile crystals are formed indicating that nucleation is relatively slower than the growth rate thus forming rod shaped nanoparticles with linearly packed TiO_6 octahedral units which exhibits less strain on the particles.

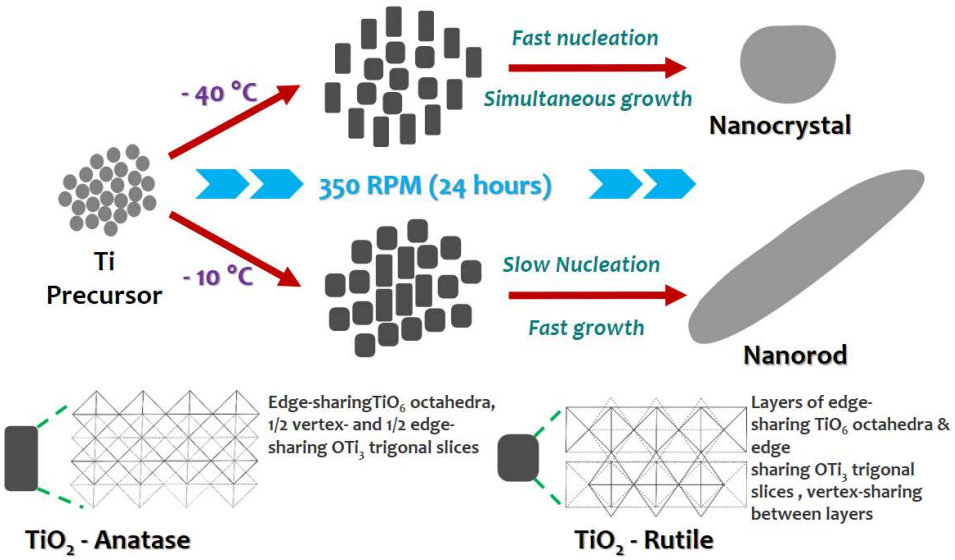

Figure 3.2 : Schematic illustration of TiO_2 synthesis process

Where at -40°C, growth occurs simultaneously with fast nucleation leading to anatase phase with zigzag packed crystal structure as also reflected from high strain on the particle surface. This probably explains the formation of nanorods and nanocrystals with phase transition from anatase to rutile at sub-zero synthesis temperatures.

3.1.2 Crystallographic analysis of titania by XRD and RAMAN

The morphologies of nano-TiO_2 were characterized by XRD as shown in Figure 3.3 Interestingly, the peaks in Figure 3.3 are broader which indicates the formation of small size particle. The XRD data of all TiO_2 are mainly consists of two peaks which governs their crystallographic phases, 2θ = 25.33° and 27.24° corresponding to anatase (101) and rutile (110) and are matching with JCPDS reference spectra of TiO_2 anatase 21-1271 (tetragonal) and TiO_2 rutile 21-1276 (tetragonal) respectively.

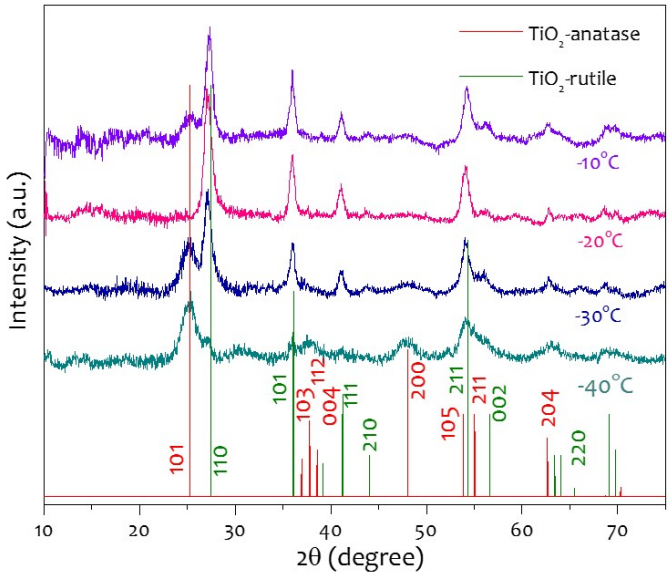

Figure 3.3 : XRD pattern of nano-TiO_2 synthesized at -40°C to -10°C where planes at (101) and (110) represents anatase and rutile phase respectively

As the reaction temperature increases from -40 to -10°C, significant changes in the XRD pattern of all TiO_2 samples were observed. From -40 to -20°C, (101) plane reportedly decreases

in intensity, in contrast to (110) plane. Whereas further increases in temperature from -20 to -10°C, (110) plane shows decreased intensity while (101) plane intensity increases. Such variation in planar intensities indicated the effect of temperature on the indicate change in the size and phase percentile in the product.

Raman analysis as shown in Figure 3.3, indicated the presence of both anatase and rutile Raman vibrational modes. TiO_2 prepared at -40°C display Raman active peaks having highest intensity peak (e_g) at 150 cm^{-1} and other peaks (a_{1g}, e_g and $2b_{1g}$) suggesting towards high percentage of anatase phase as shown in Figure 3.3. However, the TiO_2 sample prepared at -20°C confirms the high percentage of rutile phase showing (e_g and a_{1g}) Raman active peaks at 443 cm^{-1} and 608 cm^{-1} respectively. The peak at 254 cm^{-1} is due to multiple phonon scattering process known as compound vibrational peak [Mali, *et al.*, 2011]. The strain present on the grain boundaries, oxygen vacancies, temperature, particle size etc. are known to directly influence the Raman peaks [Wang, *et al.*, 2008]. A small shift in band positions might be due to phonon confinement, lattice strain, crystalline size and oxygen defects [Ocaña, *et al.*, 1988]. The crystallographic phases of both TiO_2 analyzed by Raman spectroscopy are in accordance with the above XRD findings and revealed the presence of both anatase and rutile crystallographic phases in both the samples. Anatase TiO_2 consists of the space group I4/amd (D4h 19) and it is assisted by two TiO_2 units in the *Bravais cell*. These crystals show the present lattice vibrations at the *Brilliouin zone* [Zhang, et al., 2000].

$$\Gamma = a_{1g} + a_{2u} + 2b_{1g} + b_{2u} + 3e_g + 2_{eu} \quad (3.1)$$

The a_{1g}, $2b_{1g}$ and $3e_g$ are Raman active modes whereas the remaining three are infra-red active [Zhang and Banfield, 2000]. Rutile TiO_2 consists of the P4/mnm (D_{4h}^{14}) structure and lattice vibrations at K=0 in Brilliouin zone given as

$$\Gamma = a_{1g} + a_{2g} + a_{2u} + b_{1g} + b_{2g} + 2b_{1u} + e_g + 3e_u \quad (3.2)$$

The four vibrations a_{1g}, b_{1g}, b_{2g} and $3e_g$ are Raman active modes [Zhang, *et al.*, 2006].

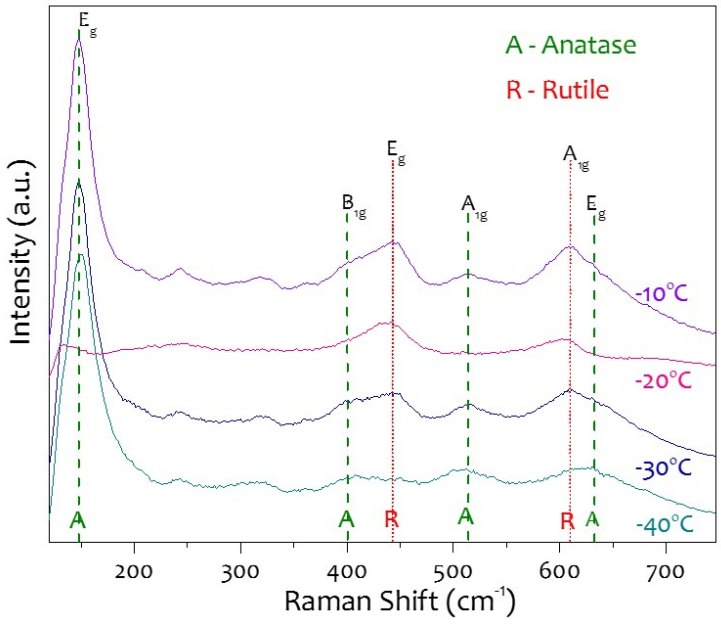

Figure 3.4 : Raman analysis of nano-TiO_2 synthesized at -40 °C to -10 °C

The XRD analysis was used to find out the weight percentage of phases in the synthesized TiO_2. The percentage of rutile and anatase in TiO_2 were calculated using the following equation [Prabhu, *et al.*, 2014].

$$WR = \frac{IR}{(0.884IA + IR)} \quad (3.3)$$

where WR is a *percentage of rutile*, IR and IA are the *diffraction intensities peak* of rutile (110) and anatase (101) respectively. The magnitude of the IR and IA were calculated by

Gaussian fitting of these peaks [Prabhu, Rao, Kumar and Kumari, 2014]. The values of IR and IA of different TiO_2 are inserted into the above equation and the relative WR of various TiO_2 synthesized from -40°C to -10°C are listed in Table 3.1.

As shown from XRD pattern and Table 3.1 the diffraction peak of TiO_2 synthesized at -40 °C is broad and corresponds to both 58% anatase and 42% rutile phases. The broad diffraction peaks indicate towards the formation of defects on amorphous grain boundary with small particle size. These defects produce strain in grain boundaries and decreased the growth of the nanocrystalline particles. With significant increment in weight percentage of rutile phase (63%), TiO2 synthesis at -30°C shows that anatase is converted into rutile phase with increased crystal size due to lower defects. At -20°C, a significant amount of anatase is converted into rutile phase (79%) without any absolute defects.

Table 3.1 : Different parameters of TiO_2 nanoparticles synthesized from -40°C to -10°C

TiO_2 Synthetic temperatures (°C)	Weight % of R	Weight % of A	Crystallite size (nm)				Lattice strain	Band gap (eV)
			Williamson-Hall plot	TEM	Rietveld			
					R	A		
-40	42	58	4.4	3.9	2.8	2.7	0.0367	3.02
-30	63	37	10.0	4.9	8.6	4.7	0.0348	2.98
-20	79	21	10.4	9.4×38.8*	9.0	2.8	0.0300	2.92
-10	73	27	13.8	4.6×16.5*	9.2	4.3	0.0323	2.97

* Dimension for nanorods are in width×height

The gain in anatase phase indicates linear increment in defects at the grain boundary that generates lattice strain and accelerate grain growth. The *pseudo-Voigt function*, *Rietveld refinement*, and *Warren-Averbach* analysis were mostly used to estimate the crystallite size and lattice [40-42].

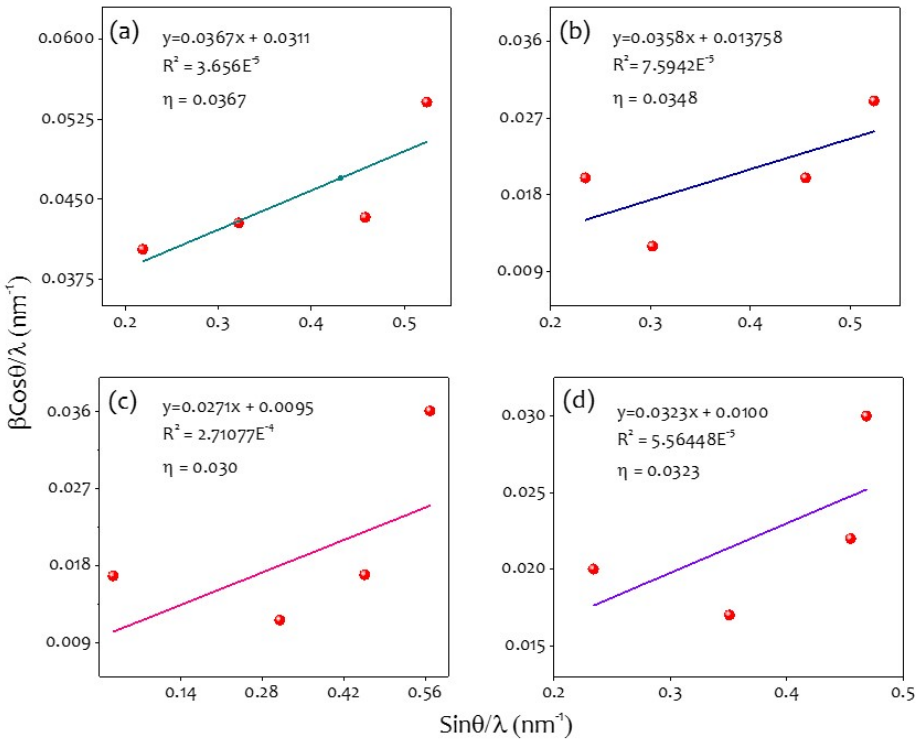

Figure 3.5 : (a) to (d) Willamson–Hall plot of nano-TiO_2 synthesized at -40°C to -10°C respectively

In *Williamson-Hall* (W-H) analyzes both strain and size induced broadening and are deconvoluted by evaluating the peak width with respect to θ. It is also a simplified integral breadth method to derive both parameters [Qin and Szpunar, 2005]. By using *Williamson-Hall equation*, lattice strain is calculated for all the synthesized TiO_2.

$$\frac{\beta\cos\theta}{\lambda} = \frac{1}{(D)} + \eta\frac{\sin\theta}{\lambda} \tag{3.4}$$

In the above Eq. (3.4), β is the *full-width half maximum* (FWHM) and θ is *half the diffraction angle* of the diffraction peaks of rutile, anatase and rutile-anatase mixed phases. λ is the *wavelength of X-ray*. Where D is the *crystal size* and η is the *value of lattice strain*. A graph having linearly fitted X axis as βcosθ/λ and Y axis as sinθ/λ is plotted (shown in Figure 3.5). Effective lattice strain is calculated by the slope. The Eq. (3.4) was used to calculate the crystalline size of all samples. The same equation represents a uniform deformation model (UDM) assuming uniform strain in all crystallographic directions. Crystallite size calculated by the Rietveld and Williamson-Hall analysis are provided in Table 3.1. As seen from the values, the crystallite size obtained by Rietveld analysis are slightly lower than Williamson-Hall due to instrumental factors were taken into account for correcting peak broadening [Kumar, *et al.*, 2013].

The calculated lattice strain of all TiO_2 samples are compiled in Table 3.1 and Figure 3.5 shows the Williamson-Hall plot of each sample with error values as R^2 (residual square). The lattice strain of -40 and -30°C are found to be as 0.0367 and 0.0348 receptively. The increased lattice strain at these temperatures is due to the presence of defects in the grain boundary with comparatively more number of atoms in the boundary. These two factors were able to produce stress in the grain boundaries. And it also increases strain in the system [Moghaddam and Nasirian, 2012]. The defects are gradually reduced where crystalline size increases respectively. At -20 and -10°C, the synthetic process favors the formation of wide particles, with observed high weight percentages of rutile phase. The increased crystalline sizes were able to reduce defects in grain boundaries, resulting in the reduced lattice strain [Tauc, *et al.*, 1966]. Therefore, the synthetic temperature has the main role along with other factors in the anatase to rutile phase transformation. Specific synthesis temperatures like -20 and -10°C efficiently favors the slower nucleation rate than growth, leading to the formation of larger particle size along with high weight percentage of rutile phase. There are also few reports stating that the phase change depends on the packing density. For phase conversion to anatase, small crystalline size particle requires less activation energy. Small size nanoparticles have more interaction with a large number of nanoparticles around them which favors the chances of better interface nucleation. So by varying synthesis temperature for all TiO_2, it can be observed that TiO_2 are very sensitive to the synthesis temperature, and change in phase was observed by interface nucleation. Especially at -20 and -10°C this phenomenon supports the change in weight percentage of rutile phase.

3.1.3 Crystalline nature and optical properties of titania by TEM and UV-vis spectroscopy

The size and morphology of all TiO_2 were analyzed by HRTEM. The TEM images Figure 3.6 reveal that the nanoparticle synthesized at various temperature were morphologically different from each other. Those TiO_2 synthesized at -40 and -30°C were in an oval shape with average particle size of 3.9 and 4.9 nm respectively. Whereas at -20 and -10°C nanoparticles were in a rod shape. With the increasing temperature from -20 and -10°C, nanorods average width reduces from 9.4 to 4.6 nm and average length also decrease from 38.8 to 16.5 nm.

The variation in particle size and its shape were mainly governed by the rate of the nucleation and growth. Narrow size particle distribution can be obtained, when nucleation rate is greater than the rate of new precursor formation. In such condition nucleation and growth cannot occur simultaneously and particle shows growth in all direction, observed at -40 and -30°C.

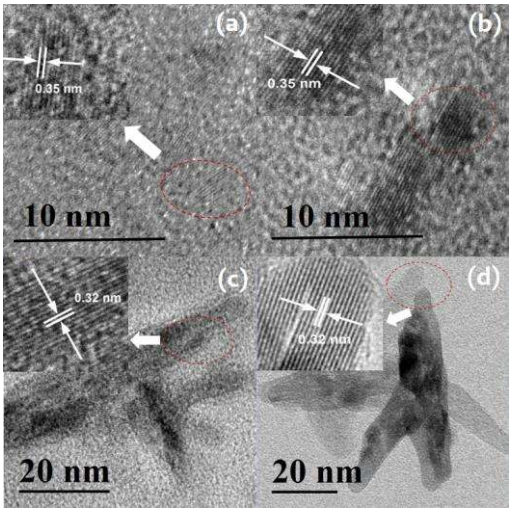

Figure 3.6 : (a) to (d) TEM and HRTEM showing nano-TiO_2 synthesized at -40°C to -10°C respectively

In the same way, if the rate of new precursor formation is greater than the nucleation rate, then the precursor concentration remains more and nucleation takes place simultaneously. In such condition, wide range distribution was observed at -20 and -10°C, older nuclei will grow bigger compared to the younger ones and favours the growth is in one direction. It has significant importance to obtain nanorods and nanocrystals with very small sizes at these sub-zero synthetic temperatures in high-performance solar cells and photocatalysis field.The HRTEM image of -40°C and -10°C showing inter planar distance with anatase and rutile as dominating phase, respectively and respective dominating phases were also observed in SAED pattern of -40°C and -10°C shown in Figure 3.7.

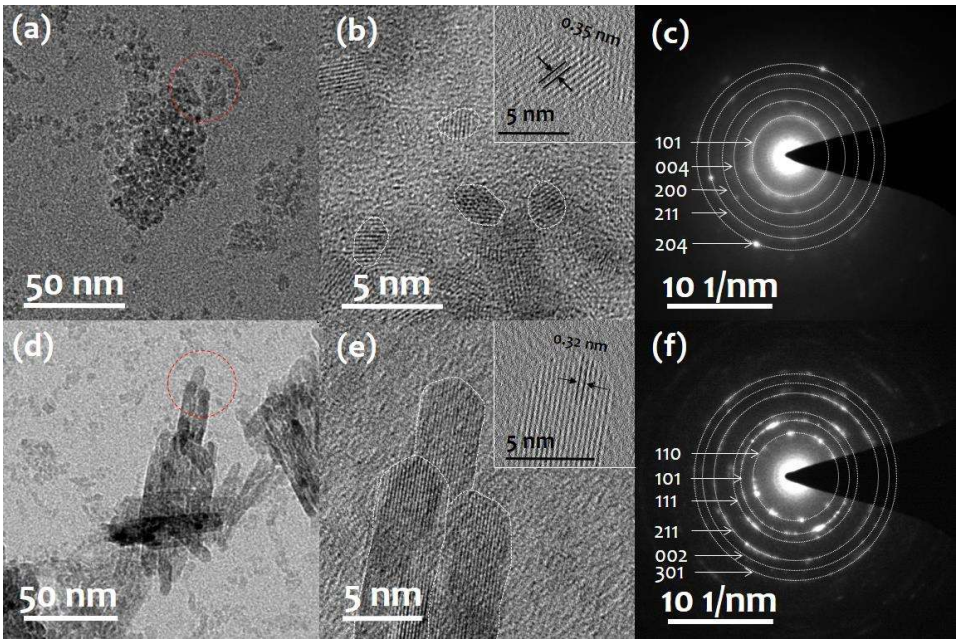

Figure 3.7 : (a) and (b) TEM images, (c) and (d) HRTEM images with marked inter planar distance and (e) and (f) are SAED pattern of -40 °C and -10 °C respectively. Dotted lines in (e) and (f) are guide to eye

The Brunauer–Emmett–Teller (BET) measurements of nano-titania were performed for the samples prepared from -40 and -10°C for observing the maximum surface area due to change in morphology. As shown in Figure 3.8, the sample prepared at -40°C temperature (oval shaped), surface area of 135 $m^2\ g^{-1}$ was obtained in contrast to the rod shaped nano-TiO_2 (prepared at -10°C) with surface area of 100 $m^2\ g^{-1}$. The higher surface area of the oval shaped

nano-titania is as expected due to high surface to volume ratio for oval particles as compared to nanorods.

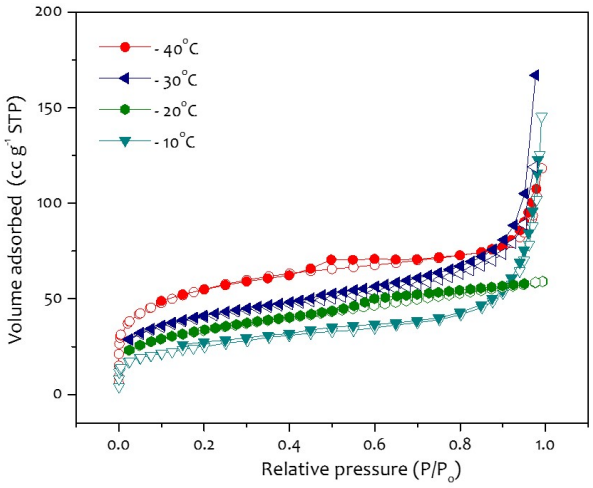

Figure 3.8 : N_2-adsorption–desorption isotherms of nano-TiO_2 prepared at -40 °C and -10°C

Optical properties of various synthesized TiO_2 have been performed as quantitative analysis of the band gap, the absorption coefficient of all TiO_2 were calculated from the reflectance data. Optical band gap of all TiO_2 were obtained using relational expression given by *Tauc et al.* [Tauc, *et al.*, 1966].

$$(h\nu F(R\infty))^{(1/n)} = A(h\nu - Eg) \quad (3.5)$$

Where A is *proportional constant* depends on the properties of the material, h is the *Planck's constant*, ν is the *frequency of vibration*, Eg is the *band gap*, F (R∞) is a *Kubelka-Munk function* and n is *constant* and it is directly related to the nature of samples electronic transition. For allowed direct transition value of n is 1/2, allowed indirect transition value of n is 2, forbidden direct transition value of n is 3/2, and for forbidden indirect transition value of n is 3. Since TiO_2 shows allowed indirect transition, so the value of n = 2 was used in Eq. (3.5) for all TiO_2. The recorded diffusion spectrum is converted *to Kubelka-Munk function* [Valencia, *et al.*, 2009].

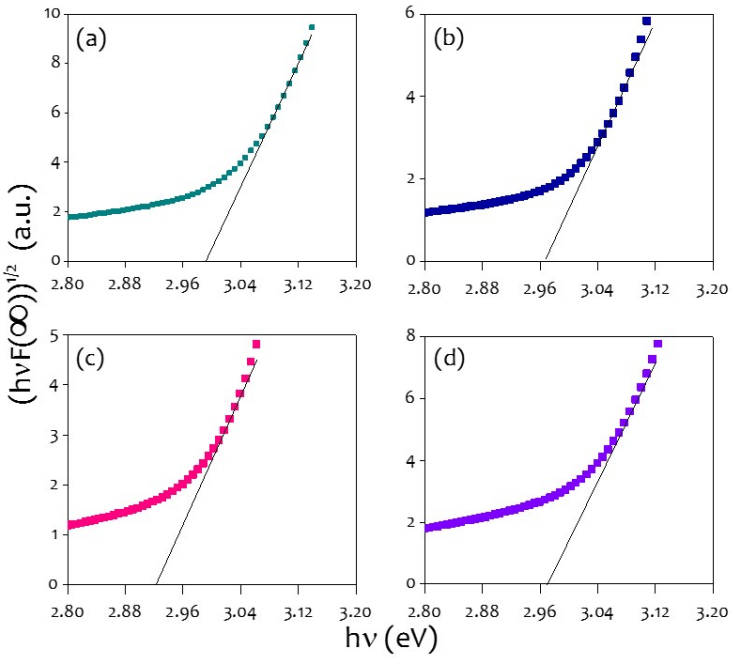

Figure 3.9 : (a) to (d) hν and $(h\nu F(R\infty))^{(1/2)}$ plot of nano-TiO_2 synthesized at -40°C to -10°C respectively

$$F(R\infty) = \frac{(1 - R)^2}{2R} \quad (3.6)$$

Where, F (R∞) is a Kubelka-Munk function which is proportional to the *absorption coefficient* (α), and R is the *reflectance* of a given wavelength. Thus for actual experimental Eq. (3.5) becomes

$$(h\nu F(R\infty))^{(1/2)} = A(h\nu - Eg) \quad (3.7)$$

Using the F (R∞), the curve is drawn having a value of $(h\nu - (h\nu F(R\infty))^{(1/2)})$, with the help of hν and $(h\nu F(R\infty))^{(1/2)}$ as X and Y axis respectively. Here hν is calculated using $E = hc/\lambda$ where, E is a *photon energy*, h is *Planck's constant*, c is the *light intensity* and λ is a *wavelength*.

The calculated optical band gaps are shown in Figure 3.9 and summarized in Table 3.1. It can be observed from variation in weight percentage of rutile that as the synthesis temperature increases from -40°C to -20°C there is a simultaneous reduction in optical band gap from 3.02 to 2.92eV. The weight percentage of rutile phase has a direct impact on the band gap of TiO_2. As earlier discussed, at -20°C and -10°C temperatures, the nucleation rate is lower than the growth rate, which helps to change phase from anatase to rutile. Due to the high weight percentage of rutile, TiO_2 synthesized at -20°C and -10°C possesses optical band gaps of 2.92 to 2.97eV respectively. These changes in the optical band gap with respect to synthesis temperature can be attributed to the stress produced in the grain boundaries which is due to the presence of defects and particle size [Yu, *et al.*, 2002]. It is mandated that the variation in interatomic distances can alter the optical band gap indicated by weight percentage of anatase and rutile, and the particle sizes have a significant impact on the band gap, directly governed by the TiO_2 reaction temperature.

3.2 ELECTRON TRAPPER ZnO-TiO_2 HETEROJUNCTION SOLID NANOSPHERES

Titania and zinc oxide are the most explored metal oxide semiconductors and have been extensively used in various applications like environmental detoxification, sensing, solar cells and photocatalysis [Pan, *et al.*, 2014; Lü, *et al.*, 2010]. Over the past decades, composite, layered structure, doping, and various nano-morphologies of TiO_2/ZnO have been extensively studied [Rani and Tripathi, 2015; Idígoras, *et al.*, 2016; Ling, *et al.*, 2013]. Despite wide applications of TiO_2/ZnO composite, drawbacks like charge recombination, lower surface area and electron transport make their use cumbersome [Chandiran, *et al.*, 2014; Dahl, *et al.*, 2014]. The heterojunction of ZnO and TiO_2 semiconductor is one of the efficient way to solve these issues by generating a highly porous surface for the electron trapping, but limited efforts have been made to enhance electron transport due to non-functional interface between heterojunction [Yu and Ran, 2011]. A good heterojunction should possess matching band levels for high electron mobility and conductive interface [Lü, Huang, Mou, Wang and Xu, 2010]. The heterojunction of TiO_2 and ZnO with similar band structure usually formed the II-type heterojunction with high mobility due to improved charge isolation compared to their pure oxides and reduce the recombination during charge separation. It has been reported that Ti-doped ZnO showed high conductivity and high surface area which are important for electron trapping. ZnO has higher electron mobility (205–300 $cm^2\ Vs^{-1}$) than TiO_2 ($10^{-5}\ cm^2\ Vs^{-1}$) [Park, *et al.*, 2010; Zhang, *et al.*, 2009] and thus ZnO-TiO_2 heterojunction with appropriate architecture and optimal doping can facilitate electron trapping. Various architecture of both oxides in the form of nanotubes, nanowires, clusters, hollow spheres, core shell and 3D hybrid arrays have been explored for enhanced charge transport [Kuang, *et al.*, 2008; Abedi and Morsali, 2015]. Unfortunately, de-trapping due to random electrical paths, surface states and defects in some cases hinder their application in DSSC. Compared to the other architectures solid nanosphere structure which is reported for the first time in this study is shown to exhibit higher internal surface area, enhanced light scattering ability and more sites for dye anchoring. The highly porous, microsized volume spheres significantly enhances total surface area of the film [Jung, *et al.*, 2013].

3.2.1 Mechanism and morphological analysis of ZnO-TiO_2

The 0, 1, 5 and 10% ZnO doped TiO_2 solid nanospheres were synthesized by solvothermal crystallization reaction.

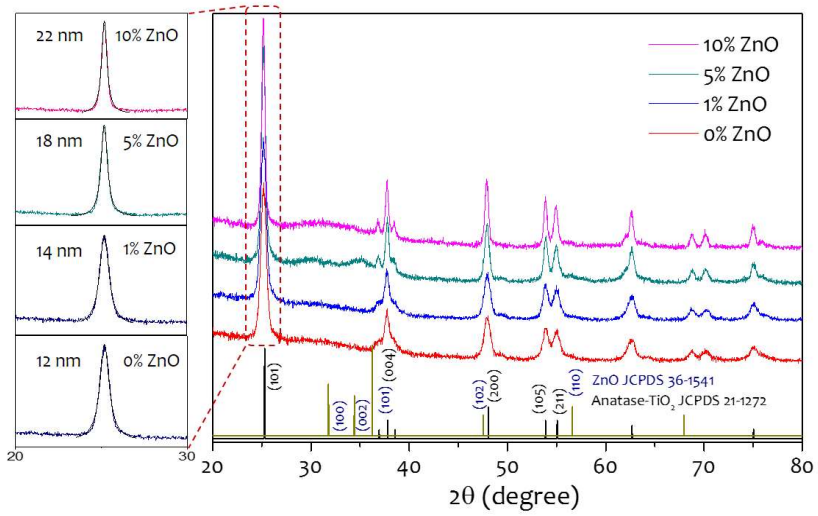

Figure 3.10 : XRD patterns of the TiO_2 doped with ZnO of varying weight percentage (0, 1, 5 and 10%). The inset on right side shows the respective (101) peak used for fitting and particle size calculation

Firstly, TiO_2 precursor beads are synthesized by hydrolysis of titanium tetra-isopropoxide followed by addition of different amount of Zn acetate dehydrate precursor during the solvothermal reaction resulting in a hybrid nanostructure of ZnO-TiO_2 solid nanospheres. In X-ray diffraction analysis (shown in Figure 3.10), all the diffraction peaks of XRD patterns correlate with anatase phase of TiO_2 (JCPDS 21-1272). However, the crystallinity of the TiO_2 solid nanosphere improves with ZnO%, and resulted in relatively higher peak intensity [Huang, *et al.*, 2012]. The average crystalline size for TiO_2 solid nanosphere was calculated using *Debye-Scherrer equation* [Holzwarth and Gibson, 2011] to be ~12 nm which increased to ~22 nm for 10% ZnO doping as shown in inset of Figure 3.10, left.

The X-ray photoelectron spectroscopy (XPS) was carried out to analyse the chemical composition and oxide species of the ZnO doped TiO_2 solid nanospheres. The full range spectra showed the presence of Ti 2p, O 1s and Zn 2p as shown in Figure 3.11a and respective binding energy values are summarized in Table 3.2. The spin-orbit components of Zn $2p_{3/2}$ and Zn $2p_{1/2}$ shows binding energy values at around 1021 and 1044 eV respectively, and splitting of 23 eV indicates that Zn ions exist mainly as Zn^{2+} chemical element state due to the formation of ZnO (Figure 3.11b) [Marcì, *et al.*, 2001]. The intensity of Zn 2p peak increases up on increasing ZnO%, however, the peak position of Zn 2p exhibits a notable shift by ~0.5 eV towards higher BE value on introduction of ZnO.

Table 3.2: The surface analysis parameters and atomic ratios calculated from XPS spectra

ZnO % in TiO_2	*Binding energy (eV)*						Atomic % Zn/Ti
	Zn $2p_{3/2}$	Zn $2p_{1/2}$	Ti $2p_{3/2}$	Ti $2p_{1/2}$	O 1s (O^{2-})	O 1s (OH^-)	
0	-	-	458.6	464.4	530	532.2	-
1	1022.1	1045.2	458.6	464.4	530	530	0.04
5	1021.6	1044.8	458.4	464.2	529.7	531.8	0.14
10	1021.5	1044.7	458.4	464.2	529.6	531.7	0.2

This clearly indicates that Zn^{2+} persist more in the solid nanosphere lattice rather than undergoing phase separation. The Ti 2p spectra are quite similar to typical Ti^{4+} in the form of

TiO_2 [Allam and El-Sayed, 2010]. The effect of ZnO on Ti 2p spectrum is visible by the shifting of Ti 2p peak by 0.2 eV to lower BE values as shown in Figure 3.11c.

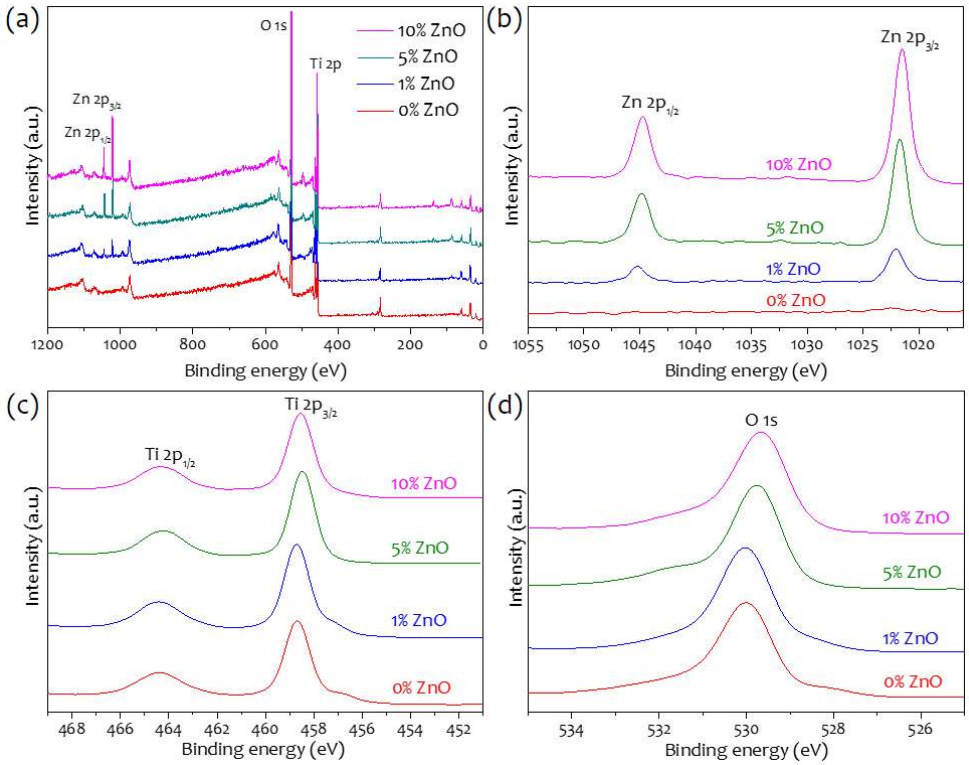

Figure 3.11 : (a) Full range XPS survey spectra, high resolution spectra of (b) Zn 2p, (c) Ti 2p and (d) O 1s of TiO_2 solid nanospheres with different ZnO doping

The reason causing this BE difference may be due to the interface between ZnO and TiO_2 nanoparticles. The broadness of O 1s spectra (Figure 3.11d) indicates the presence of several kind of oxygen species with O^{2-} appearing at 530 eV and OH^- species at 531 eV. In all samples, the Zn/Ti atomic ratio is less than the 1 (Table 3.2), which infers random distribution of ZnO all over the TiO_2 solid nanosphere [Hwang, *et al.*, 2011]. The O 1s peak of ZnO-TiO_2 solid nanosphere shifts due to Zn-O-Ti complex bond formation at the interface.

3.2.2 Crystalline nature and elemental analysis of ZnO-TiO_2 heterojunction solid nanospheres

The influence of the ZnO wt% on the structure and surface morphology of TiO_2 solid nanospheres shown in Figure 3.12. The FESEM images in Figure 3.12a-d illustrate the porous nature of these nanostructures, formed by the aggregation of the nanocrystallites of TiO_2 and ZnO. As can be seen from the images, the porosity is greatly influenced by ZnO doping. With increasing amount of ZnO, the TiO_2 solid nanospheres begin to disintegrate with the decrease in its average sphere size from 600±20 to 200±30 nm. The detailed structure of the solid nanosphere was investigated by TEM images as shown in Figure 3.12e-h. Interestingly, the solid spheres are no longer packed with monodisperse nanocrystallites, however, it consists of polydisperse aggregates. Moreover, there is a gradual increase in crystallite size of TiO_2 with increasing ZnO% resulting in smaller pores at the surface of the solid sphere.

A typical TEM image of 5% ZnO in TiO_2 sample was chosen for detailed TEM study as shown in Figure 3.13a. The HRTEM image (Figure 3.13b) is taken from a selected area marked in Figure 3.13a which shows lattice planes with two different d-spacing. The d-spacing of 0.35 nm corresponds to (101) anatase TiO_2 while the other value of 0.26nm matches well with the (002) wurtzite structure of ZnO.

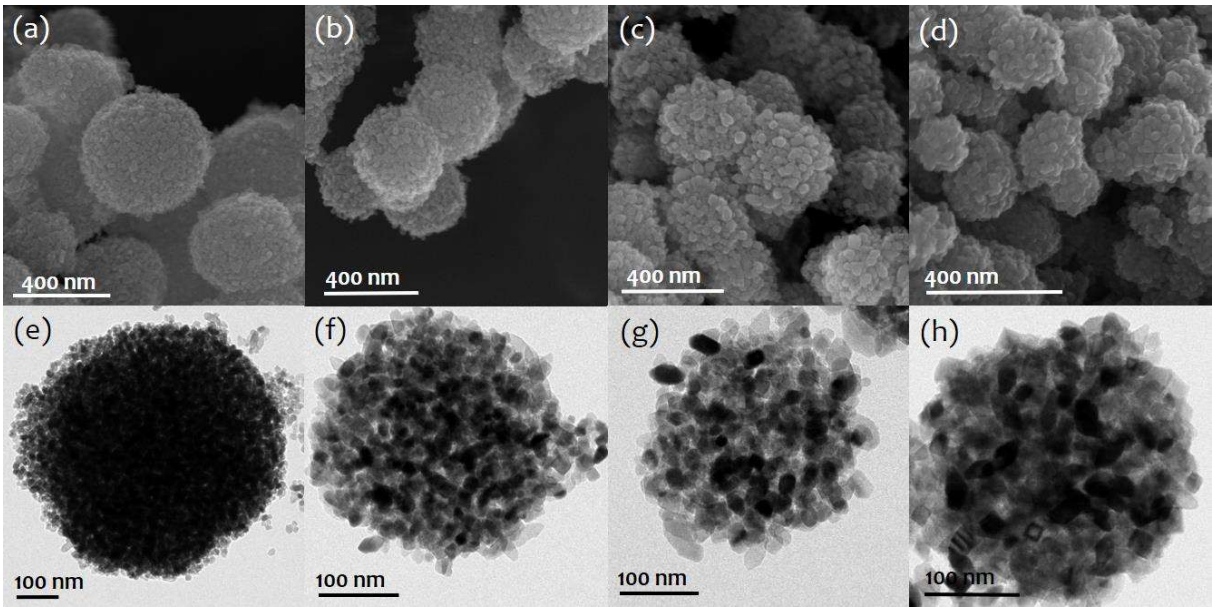

Figure 3.12 : (a-d) FESEM images and (e-h) TEM images of TiO_2 solid nanosphere doped with ZnO of 0, 1 ,5 and 10% by weight respectively

Since no transitional layer was found at the interface between the ZnO and TiO_2 and the distinct boundary of nanocrystals indicate that these solid nanospheres are a mix of both nanostructures. In the ED pattern, only anatase TiO_2 is visible (Figure 3.12c) and ZnO is absent due to the lower weight % of ZnO. Figure 3.12d, e and f confirm the compositional homogeneity of the solid nanosphere by the random distribution of Ti, Zn and O elements. Electron Dispersive X-ray (EDX), elemental distribution is summarized by bargraph in Figure 3.13g.

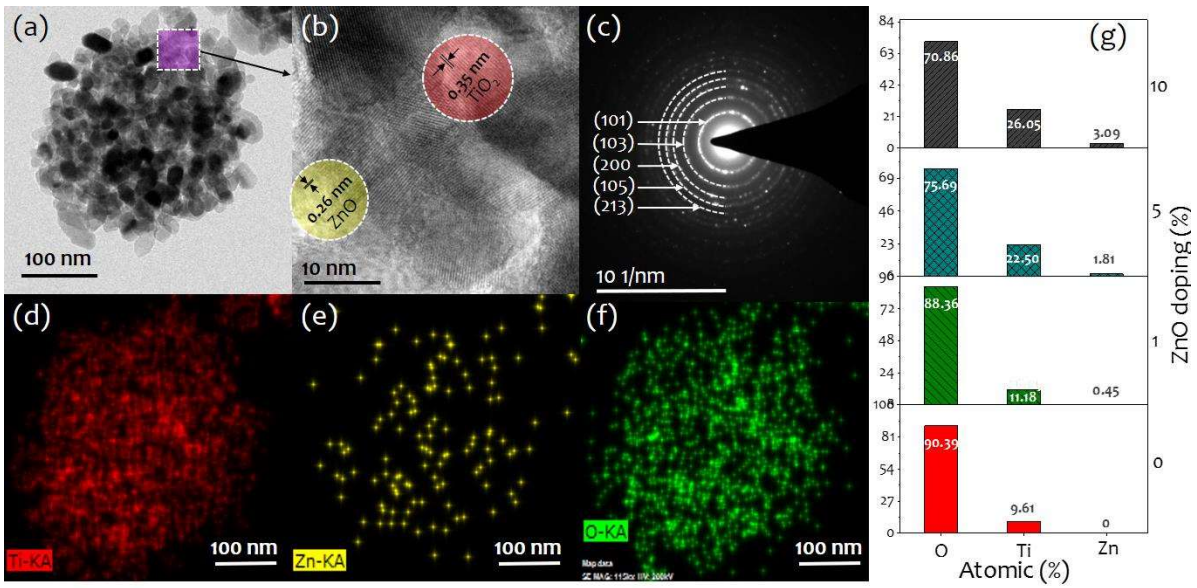

Figure 3.13 : (a) TEM image, (b) HRTEM image and (c) ED pattern of TiO_2 solid nanosphere with 5% ZnO doping. (d-f) EDS maps of Ti K (red), Zn K (yellow) and O K (green). (g) Bar graph displaying atomic % obtained from EDS spectra by varying the ZnO doping levels

The Zn atomic % gradually increases from 0 to 3.09% with increasing amount of ZnO doping. The mismatch between doping amount and atomic % controls the growth behavior of ZnO/ TiO_2 solid nanosphere [Bouchet, *et al.*, 2003]. The Zn ions have a tendency to segregate in anatase TiO_2 crystal lattice only if their doping concentration (atomic) is < 0.1%. This is a result of significant difference in charge and atomic properties between Ti and Zn ions, which apparently hinder the incorporation of Zn ions into TiO_2 lattice, and further responsible for the

mismatch between the actual weight % and precursor doping %, resulting in the heterojunction crystallite formation of ZnO-TiO_2 solid nanospheres [Chen and Shen, 2009].

3.2.3 Specific surface area study of ZnO-TiO_2 nanospheres

The adsorption-desorption isotherms of the ZnO doped TiO_2 solid nanosphere are shown in Figure 3.14a.

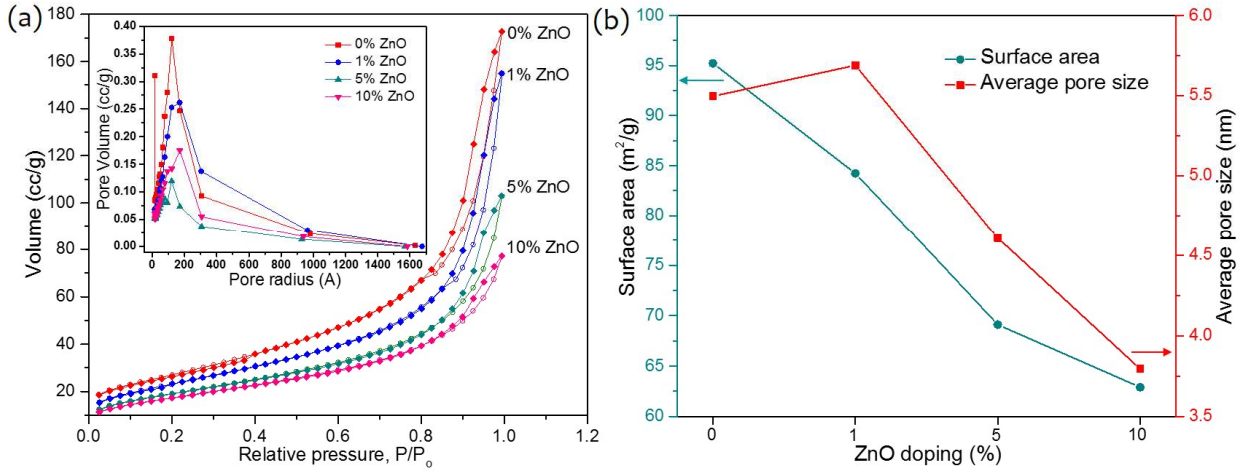

Figure 3.14 : (a) N_2 adsorption-desorption BET isotherm of TiO_2 solid nanospheres with different ZnO doping. (b) Effect of varying ZnO doping level on surface area and average pore size

The shape of the curve corresponds to a type-IV isotherm which is characteristic of the mesoporous structure and the observed hysteresis suggests the presence of small pores as observed loops were not shifted to a high relative pressure [Yu, *et al.*, 2006]. The specific surface area obtained from BET analysis shows a gradual but linear decrease from 95.23 m^2/g to 63 m^2/g (Figure 3.14b), however, the overall surface area is still higher in comparison to P25 (51 m^2/g) [Yu, *et al.*, 2007]. The average pore size was calculated by BJH analysis for different doping percentage and their distribution were shown in inset of Figure. 3.14a. Most interestingly, the average pore volume increases for 1% doping of ZnO in TiO_2 while it decremented stepwise for higher doping levels. This deviation from decreasing trend is observed since the size of the pores formed in TiO_2 solid nanosphere are relatively of the size of ZnO aggregate [Tang, *et al.*, 2004]. The average pore size decreases on increasing ZnO content beyond 1%. This may be due to the bigger grain size for higher ZnO% as shown in the TEM images in Figure 3.12.

3.3 HYDROGENATED TiO_2 AND HfO_2 NANODOTS

Energy harvesting via sun is a global challenge that require efficient and robust solar active materials. The performance of DSSC depends on the trade-off between light harvesting efficiency and charge collection across the photoanode. Much of the contemporary research focuses around tailoring the properties of TiO_2 by different approaches that include altering the morphology, tuning the phase or by external doping [Tian, *et al.*, 2011; Roose, *et al.*, 2015]. In order to increase the charge collection ability, TiO_2 is synthesized in one-dimensional morphologies such as nanorods and nanotubes, apart from mesospheres and nanospheres. Although one-dimensional TiO_2 nanorods and nanotubes provide a highway for electron conduction, its surface area is still lower with regards to application in DSSC [Wang, *et al.*, 2012; Song, *et al.*, 2016]. Particularly, TiO_2 mesospheres and nanospheres have good light scattering ability and high surface area for greater absorption of dye that maximizes the light harvesting capability of TiO_2 thereby increasing the photocurrent generation [Li, *et al.*, 2015].

Substantial efforts have been focused on the phase tunable synthesis of TiO_2 for improving the charge recombination in TiO_2. The approach adopted for improving the optical properties of TiO_2 is by doping it with various metals, non-metals and metal oxides [Zhang, *et al.*, 2011; Ramasamy, *et al.*, 2013; Kılıç, *et al.*, 2015]. TiO_2 with a wide band gap of 3.0-3.2eV absorbs mainly in UV region (250-400 nm) which is only a part of entire solar spectrum. Thus, band gap engineering of TiO_2 is highly important for its effective utilization. For example, hydrogenation of TiO_2 lower its band gap from 3.2 to 1.8eV and enhances the solar cell efficiency by 28% [Su, *et al.*, 2015]. Doping in TiO_2 not only alters the bandgap but also helps in improving the charge transfer efficiency [Su, *et al.*, 2015]. The dielectric dopants such as HfO_2, Al_2O_3, SiO_2 and ZrO_2 introduce optical effects and are thus utilized in DSSC to curb the electron recombination process and also to decrease the electron injection resistance [Li, *et al.*, 2015; Lim, *et al.*, 2015].

3.3.1 Mechanism of hydrogenated TiO_2 and HfO_2 nanodots synthesis

The TiO_2 nanospheres doped with HfO_2 are synthesized following a slightly modified hydrothermal method as shown schematically in Figure 3.15. Typically, titanium isopropoxide precursor is hydrolysed in hexadecylamine (HDA) and aged for 18 hrs. The HDA-TiO_2 lamellar structures are usually formed upon hydrolysis of TIP. This composite tends to form micelles that polymerize resulting in the formation of mesoporous inorganic TiO_2 nanospheres [Chen, *et al.*, 2009]. Upon addition of TIP to the alcoholic medium, the clear solution instantly turned milky white giving rise to phase-separated, highly-monodispersed spherical beads. This solution is taken as a precursor for hydrothermal reaction under conditions shown in step 2, leading to the formation of crystalline TiO_2 nanospheres. The TiO_2 powder is hydrogenated by annealing at 500° C for 2 hrs under H_2 atmosphere as seen by the discoloration from white to grey black. In this work, hydrogenated HfO_2 doped TiO_2 is prepared by introducing hafnium propoxide (HIP) as hafnia precursor along with TIP (starting titania precursor) in different atomic weight ratio of 1%, 5% and 10%) following the same steps as above Figure 3.16. The doping level of HfO_2 in TiO_2 is optimized to be minimum (1%) since it is an insulating dielectric material with low electron affinity of 2.5 eV. The hydrogenated sample with 1% HfO_2 doped in TiO_2 was used for further studies

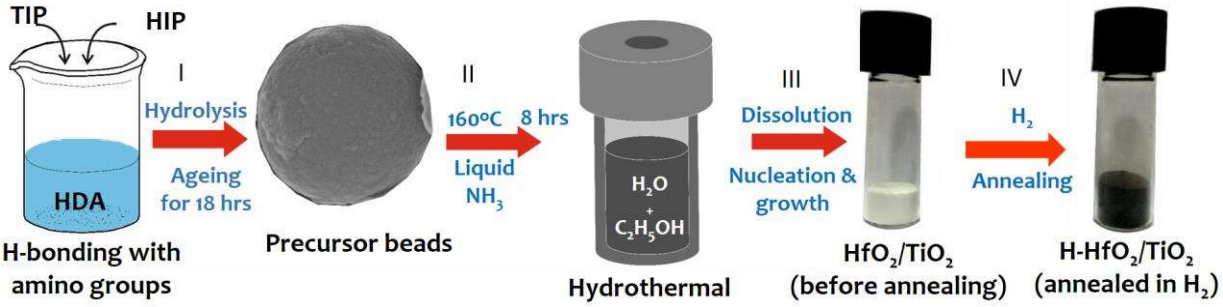

Figure 3.15 : Schematic demonstrating the synthesis method for hydrogenated TiO_2 nanospheres doped with HfO_2 nanodots

3.3.2 Morphology and structural composition of H-HfO_2/TiO_2 nanodots

The morphology and structural composition of H-HfO_2/TiO_2 were characterized as shown in Figure 3.17. Due to low doping percentage of HfO_2, no significant change in peak position was observed in XRD pattern Figure 3.18. The TEM image in Figure 3.17 indicates the formation of uniformly distributed nanospheres. The average diameter of a single nanosphere of H-HfO_2/TiO_2 is 470 ± 2nm (Figure 3.17a, inset). A nanosphere consisted of crystallites of size ~12 nm (Figure 3.17b). The HRTEM image shows the lattice spacing of 0.35 nm corresponding to (101) plane of TiO_2 anatase (Figure 3.17c). The marked area at the edge of particle exhibited Moiré pattern which was carefully examined by FFT as shown in inset of Figure 3.17c.

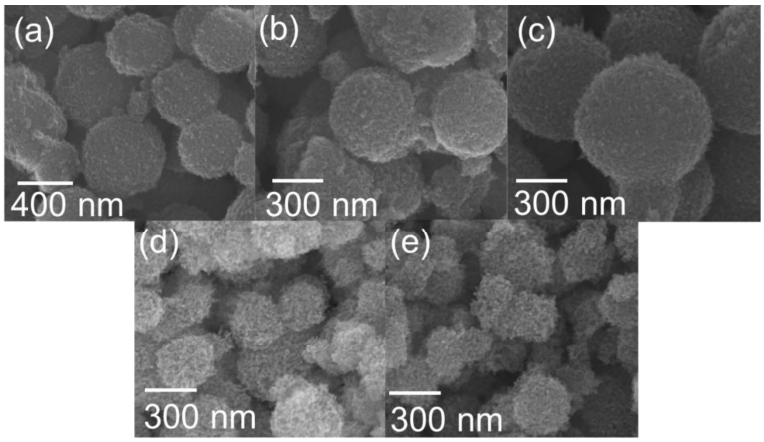

Figure 3.16 : FESEM images of (a) TiO_2 (b) 1% doped HfO_2/TiO_2 (c) 1% doped H-HfO_2/TiO_2 (d) 5% doped HfO_2/TiO_2 and (e) 10% doped HfO_2/TiO_2

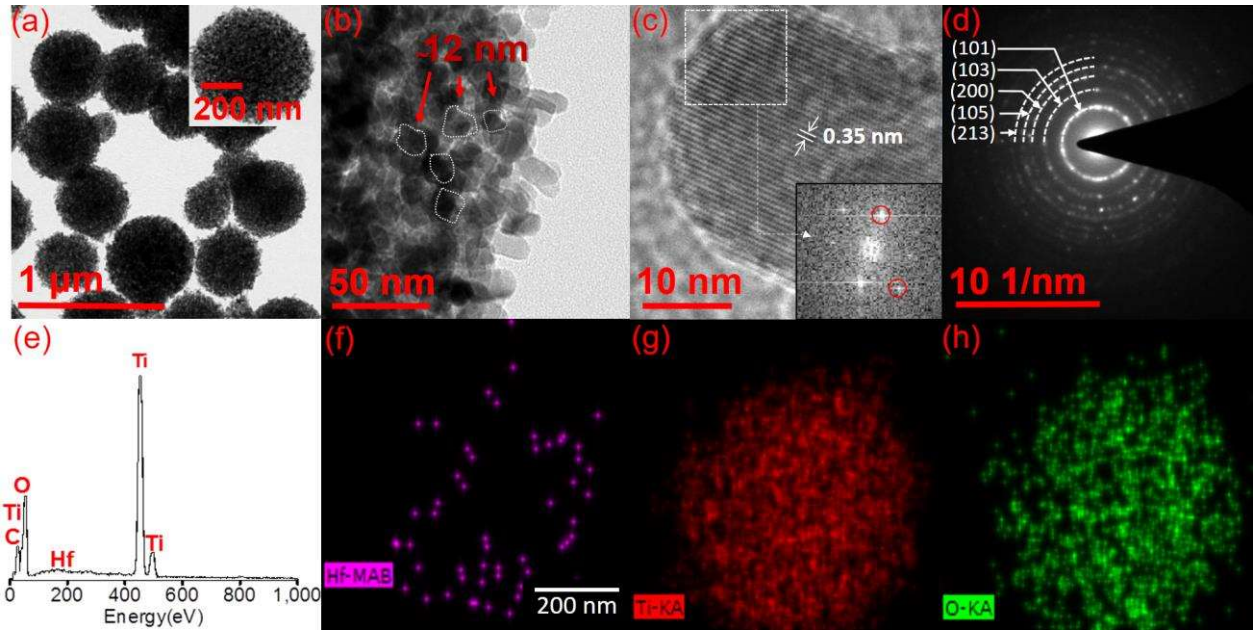

Figure 3.17 : (a) TEM images of H-HfO_2/TiO_2 and (b) a highly magnified view of H-HfO_2/TiO_2 nanosphere. (c) High resolution TEM image and (d) SAED pattern of H-HfO_2/TiO_2. (e) EDS spectrum and (f-h) EDS maps corresponding to Hf M, Ti K and O K signal respectively. Note that the signal C K in e originates from the carbon tape and can be neglected

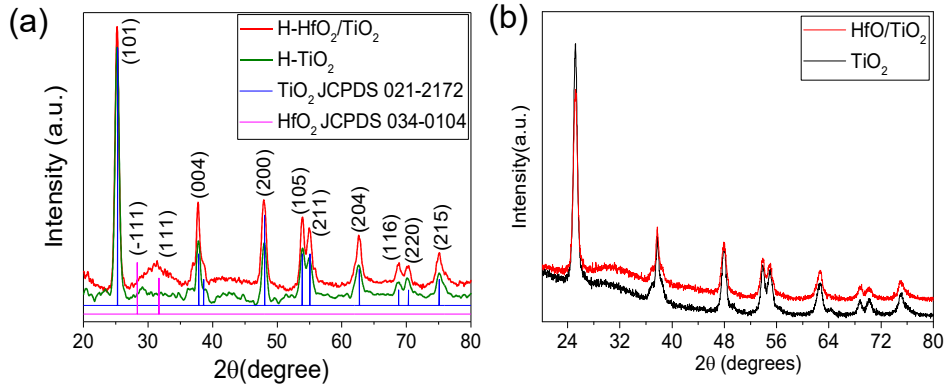

Figure 3.18 : XRD patterns of (a) hydrogenated HfO_2/TiO_2 and TiO_2 and (b) HfO_2/TiO_2 and TiO_2 without hydrogenation

The electron diffraction (ED) pattern exhibits concentric rings that are indexable to the lattice planes (101), (103), (200), (105) and (213) and corresponds to anatase phase of TiO_2 (Figure 3.17d). The HfO_2 could not be identified in ED and HRTEM however, EDS spectrum shows signals corresponding to Hf M, Ti K and O L due to the presence of HfO_2 in TiO_2 (Figure 3.17e). The EDS map of Hf in Figure 3.17e shows nanodots in the area enclosed by the TiO_2 nanosphere (Figure 3.17f and 3.17g) which infers presence of ultrasmall but monodispersed HfO_2 nanodots in TiO_2. The doping of HfO_2 nanodots as well as hydrogenation has direct influence on the optical properties of TiO_2.

3.3.3 Optical properties of hydrogenated H-HfO_2/TiO_2 nanodots

As shown schematically in Figure 3.19a, the optical path length is increased by the introduction of HfO_2 nanodots in TiO_2 resulting in higher scattering. Figure 3.19b and 3.19c shows the optical reflection spectra and corresponding band gap for TiO_2 after doping with HfO_2 and upon hydrogenation. The incorporation of HfO_2 nanodots in small quantities (1%) has little influence on the optical absorption and in turn, the optical band gap of TiO_2 (3.18 eV) as shown in Figure 3.19b. To extend the optical absorption in the visible region, the HfO_2/TiO_2 is annealed in hydrogen as shown in Figure 3.15 (step IV). Hydrogen annealing of TiO_2 is known to extend its light absorption towards visible region due to formation of sub band gap states between the conduction and valence bands with the formation of oxygen vacancy sites [Sinhamahapatra, *et al.*, 2015]. The generation of defects lead to lattice disorientation [Wang, *et al.*, 2013]. However, hydrogenation of HfO_2 in TiO_2 is not very well studied. The UV-vis diffuse reflection spectrum of HfO_2/TiO_2 is flat and featureless in the visible (400-800 nm) region, however, the reflection decreases drastically upon hydrogenation as shown in Figure 3.19b. The decrease is more than the hydrogenated TiO_2 indicating clear hydrogenation of HfO_2 as well. In case of TiO_2, band gap is known to decrease upon hydrogenation due to the presence of oxygen vacancies and Ti^{3+} sites in the crystal structure [Panomsuwan, *et al.*, 2015].

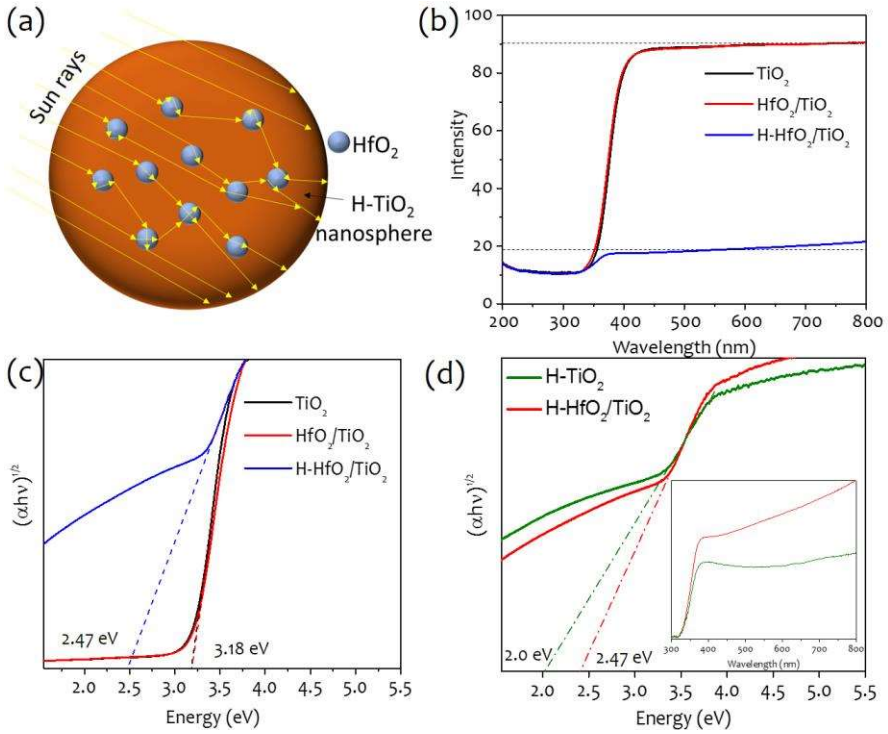

Figure 3.19 : (a) Schematic demonstrating the light interaction with HfO_2 doped hydrogenated TiO_2 nanosphere. (b) UV-vis diffuse reflectance spectra and (c) Tauc plot of $(\alpha h\nu)^{1/2}$ versus energy for band gap calculation of TiO_2, HfO_2/TiO_2 and H-HfO_2/TiO_2. (d) $(\alpha h\nu)^{1/2}$ versus energy and reflectance spectra (inset) for H-TiO_2 and H-HfO_2/TiO_2

Similarly, the optical band gap of the HfO_2/TiO_2 decreases from ~3.18 to ~2.4 eV upon hydrogenation (Figure 3.19c). The effect of HfO_2 doping on band gap is negligible under air annealed conditions, however, it is clearly visible in hydrogenated samples (Figure 3.18d). Due to the high coordination sphere of HfO_2, the defect density in H-HfO_2/TiO_2 increases as shown by the Raman spectra (Figure 3.20). There is a shift in the stretching mode of E_g peak from 146 to 151 cm^{-1} due to the induced defects and possible disorientation in the lattice structure upon hydrogenation of HfO_2 in TiO_2. The optical reflection for H-HfO_2/TiO_2 in comparison to TiO_2 (inset, Figure 3.19d) is remarkably lowered possibly due to increased optical scattering by hydrogenated HfO_2 resulting in a lowered band gap of 2.4 eV. However, in comparison to H-TiO_2 (2.0 eV), the bandgap for H-HfO_2/TiO_2 is still lower which might be important for enhancement in the visible light absorption for solar cell application.

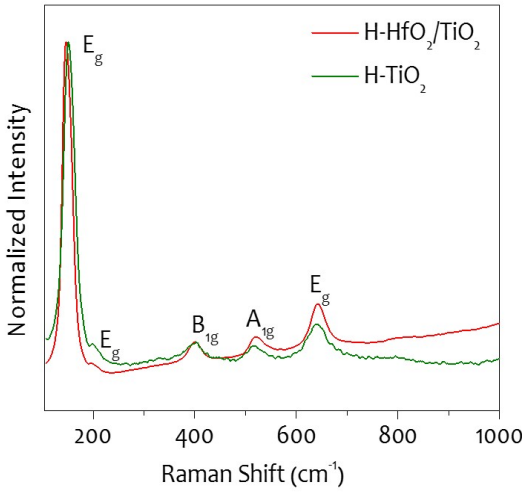

Figure 3.20 : Raman spectra of H-HfO_2/TiO_2 and H-TiO_2

The Raman spectra of H-HfO_2/TiO_2 and H-TiO_2 correspond to TiO_2 anatase phase with observed peaks at 144,197, 399, 518 and 641 cm^{-1}. These peaks correspond to E_g modes at (144, 192 and 641 cm^{-1}) and B_{1g} and A_{1g} modes at 399 and 518 cm^{-1} respectively [Zhou, *et al.*, 2014]. The highly intense peak of E_g arising at 146 cm^{-1} in the lower wavenumber indicates long range ordering in the nanocrystal [Ni, *et al.*, 2007]. The shift in the stretching mode of E_g peak from 146 to 151 cm^{-1}, is attributed to the induced defects and possible disorientation in the lattice structure upon HfO_2 doping along with hydrogenation. The E_g, A_{1g} and B_g peaks are due to the symmetric stretching, symmetric bending and antisymmetric bending vibrations of O-Ti-O [Subramaniam, *et al.*, 2014].

3.4 CONCLUDING REMARKS

This study gives a unique and simple method to prepare different phase TiO_2 nanostructures at sub-zero temperature. Sub-zero temperature induces dimension control of TiO_2 morphology and demonstrates cumulative effect of various defect densities produce strain at grain boundaries, surface area, nucleation and growth rates and band gap. Then, the hydrothermal method was explored to synthesize nanosphere. The ZnO-TiO_2 nanosphere is the first ever report on solid nanosphere compared to the other architectures. The highly porous, micro-sized volume spheres significantly enhanced the internal surface area, light scattering ability, charge transport and more sites for reaction. With the synergy of hydrogenation, HfO_2/TiO_2 nanosphere shown the good potential of doping a high coordination dielectric sphere such as HfO_2 and resulted in enhanced optical absorption and surface area.